



PAPER

Influence of chemical substitution on broadband dielectric response of barium-lead M-type hexaferrite

OPEN ACCESS

RECEIVED

8 January 2019

REVISED

23 April 2019

ACCEPTED FOR PUBLICATION

24 May 2019

PUBLISHED

12 June 2019

Original content from this work may be used under the terms of the [Creative Commons Attribution 3.0 licence](#).

Any further distribution of this work must maintain attribution to the author(s) and the title of the work, journal citation and DOI.



Liudmila N Alyabyeva^{1,9} , Victor I Torgashev^{2,10} , Elena S Zhukova¹ , Denis A Vinnik³ , Anatoliy S Prokhorov^{1,4} , Svetlana A Gudkova^{3,5} , David Rivas Góngora⁶ , Tomislav Ivek⁶ , Silvia Tomić⁶ , Nikolina Novosel⁶ , Damir Starešinić⁶ , Damir Dominko⁶ , Zvonko Jagličić⁷ , Martin Dressel^{1,8} , Dmitry A Zhrebtsov³  and Boris P Gorshunov¹ 

¹ Laboratory of Terahertz Spectroscopy, Moscow Institute of Physics and Technology (State University), 141701, Dolgoprudny, Moscow region, Russia

² Faculty of Physics, Southern Federal University, 344006, Rostov on Don, Russia

³ Laboratory of Single Crystal Growth, South Ural State University, 454080, Chelyabinsk, Russia

⁴ Prokhorov General Physics Institute of the Russian Academy of Sciences, Moscow, 119991, Russia

⁵ SEC 'Nanotechnology' Moscow Institute of Physics and Technology (State University), 141701, Dolgoprudny, Moscow region, Russia

⁶ Institut za fiziku, PO Box 304, HR-10001 Zagreb, Croatia

⁷ Institute of Mathematics, Physics and Mechanics & Faculty of Civil and Geodetic Engineering, University of Ljubljana, Slovenia

⁸ 1. Physikalisches Institut, Universität Stuttgart, D-70550 Stuttgart, Germany

⁹ Author to whom any correspondence should be addressed.

¹⁰ Sadly, our co-author and dear friend Professor Victor Torgashev passed away before the publication of this paper.

E-mail: aliabeva.ln@mipt.ru

Keywords: multiferroics, M-type hexaferrite, low-energy electrodynamics, birelaxor, terahertz, infrared, dielectric response

Supplementary material for this article is available [online](#)

Abstract

We report on the electrodynamic properties of the single crystalline lead-substituted M-type barium hexaferrite, $\text{Ba}_{0.3}\text{Pb}_{0.7}\text{Fe}_{12}\text{O}_{19}$, performed in the broad frequency range including radio-frequency, terahertz and sub-terahertz bands, which are particularly important for the development of microelectronic devices. We demonstrate how changing on a molecular level the chemical characteristics (composition, intermolecular interaction, spin-orbital interaction) of lead-substituted M-type hexaferrite influences its radio-frequency and terahertz electrodynamic response. Our results indicate a critical temperature range, $50 \text{ K} < T < 70 \text{ K}$, where significant changes of the electrodynamic response occur that are interpreted as freezing of dynamical oscillations of bi-pyramidal $\text{Fe}(2b)$ ions. In the range 5–300 K, the heat capacity shows no sign of any phase transition and is solely determined by electron and phonon contributions. An anomalous electrodynamic response is detected at 1–2 THz that features a rich set of absorption resonances which are associated with electronic transitions within the fine-structured Fe^{2+} ground state and are visualized in the spectra due to magnetostriction and electron–phonon interaction. We show that lead substitution of barium in barium hexaferrite, $\text{BaFe}_{12}\text{O}_{19}$, leads to the emergence of a pronounced dielectric and magnetic relaxational dynamics at radio-frequencies and that both dynamics have the same characteristic relaxation times, thus evidencing the bi-relaxor-like nature of $\text{Ba}_{0.3}\text{Pb}_{0.7}\text{Fe}_{12}\text{O}_{19}$. We associate the origin of the relaxations as connected with the motion of magnetic domain walls. In order to unveil crucial influence of chemical substitution on electrodynamic characteristics of the compound, we analyze our results on substituted compound in comparison with the data available for pristine barium ($\text{BaFe}_{12}\text{O}_{19}$) and pristine lead ($\text{PbFe}_{12}\text{O}_{19}$) hexaferrites. The obtained spectroscopic data on the dielectric properties of $\text{Ba}_{0.3}\text{Pb}_{0.7}\text{Fe}_{12}\text{O}_{19}$ provide insight into fundamental phenomena responsible for the absorption mechanisms of the compound and demonstrates that chemical ionic substitution is an effective tool to tune the dielectric properties of the whole family of hexaferrites.

1. Introduction

The hexagonal ferrites with the general formula $AM_{12}O_{19}$ (where $A = Ba, Sr, Pb$; $M = Fe, Al$, etc) were discovered in the first half of the 20th century [1]. Subsequently, the temperature evolution of electromagnetic, thermodynamics, mechanical, calorimetric, etc properties of the pure barium hexaferrite $BaFe_{12}O_{19}$ have been extensively investigated as described elsewhere [2]. The interest on these compounds was recently revived due to the possibility to manipulate their functional properties by inducing crystal field distortions with dopants [3–14]. In particular, the values of the coercive force [15], Curie temperature [16, 17], magnetic permeability and the dielectric permittivity reveal strong changes caused by doping and chemical substitution [18]. In addition, the non-crystalline form of the hexaferrites adds more complexity/richness to their phase diagram since the magnetic order is greatly influenced by the physical and chemical properties of the granules (impurity state, phase and granulometric composition, dispersity and granular crystal structure), which are largely influenced by synthesis method. All this make substituted barium hexaferrites promising for practical applications, such as radio-frequency absorbing coatings, magnetic recording, fabrication of permanent magnets and various components in microwave devices, telecommunication, etc. As a result, electromagnetic properties [19–25] and growth methods, such as sol–gel [26–30], co-precipitation [31, 32] and the standard ceramic method [33, 34], of these compounds are now under extensive investigations.

The goal of the present study was to explore the broad-band electrodynamic properties of $Ba_{0.3}Pb_{0.7}Fe_{12}O_{19}$ and, in particular, to unveil the influence of partial substitution of the twelve-fold coordinated cation subsystem on the barium hexaferrite crystal lattice dynamics. Though $BaFe_{12}O_{19}$ and $PbFe_{12}O_{19}$ are isostructural, the physical properties of the two compounds are drastically different in regard to the electronic configurations of the two largest cations Ba^{2+} and Pb^{2+} [35]. In contrast to Ba^{2+} ions, the outer shell of Pb^{2+} has two lone electrons, which allows nearest neighbor electronic exchange thus affecting the bond lengths; as a result the coordination environment of the Pb ions becomes strongly distorted. Pb-substituted $Ba_{1-x}Pb_xFe_{12}O_{19}$ crystals with $0.2 < x < 0.8$ revealed a large displacement ellipsoid for the mixed-occupied Ba/Pb site [35, 36]. These results are similar to what was observed by Moore and Gupta [37] for pure lead M-hexaferrite. One can thus expect that for the barium hexaferrite the ionic displacements will increase with growth of lead content. With this in mind, we have synthesized large high quality $Ba_{1-x}Pb_xFe_{12}O_{19}$ single crystals with $x = 0.7$ in order to study the induced significant changes in coordination distortions and, correspondingly, in the low-frequency/energy lattice dynamics. We stress an extraordinary relevance of hexaferrites, the compounds that reveal a unique combination of bright physical properties, like multiferroicity, quantum criticality, relaxor- and bi-relaxor-like behaviors. It is worth mentioning that despite the available thorough studies of M-type hexaferrites, their electrodynamic properties in the terahertz (THz) frequency region are still unexplored. In this paper we report on the first detailed spectroscopic study of $Ba_{0.3}Pb_{0.7}Fe_{12}O_{19}$ compound in radio, THz, far-infrared and mid infrared frequency ranges in a broad temperature interval, from 5 to 300 K.

2. Experimental

M-type barium hexaferrite single crystals $Ba_{0.3}Pb_{0.7}Fe_{12}O_{19}$ were grown by flux technique using a resistive furnace that allows the use of crucibles up to 30 ml in volume [38] with a precise temperature control. The initial charge contains stoichiometric ratio of $BaFe_{12}O_{19}$ and 80 at% of lead oxide used as flux. The starting components (lead oxides, iron and barium carbonate) were preliminarily dried for 6 h in an oven at a temperature of 400 °C. The charge of 20 g weight was then grinded in an agate mortar and loaded into a 30 ml platinum crucible that was placed in a resistive furnace and heated up to 1000 °C at a rate of 200 °C h⁻¹. The solution was held for 3 h to achieve full homogenization. For crystallization, platinum rod was used as a cooler. The temperature was decreased at a rate of 4–5 °C h⁻¹. At 900 °C the furnace was switched off. The obtained crystals were separated by boiling in a nitric acid. As a result, black crystals were obtained with characteristic hexagonal faceting of up to 5 mm.

The composition of the obtained crystals was studied using a Jeol JSM-7001F electron microscope with an Oxford INCA X-max 80 energy dispersive x-ray (EDX) fluorescence spectrometer. X-ray analysis of the samples was carried out on a powder x-ray diffractometer (PXRD) Rigaku Ultima IV using the PDXL Integrated x-ray powder diffraction software. To determine the phase composition and crystal lattice parameters, several crystals were grounded to a powder and PXRD was performed in the 2θ range 10°–90° with rate of 1°/min.

For the infrared and terahertz measurements, plane-parallel samples were cut from bulk single crystals and carefully polished, with two distinct orientations of the crystallographic c axis: parallel (x -cut) and normal (z -cut) to the sample surface. This enables optical (terahertz and infrared) measurements in polarization geometries with the electric field vector E of the probing radiation parallel and perpendicular to the c axis. Samples with thicknesses 173 (z -cut plate), 188 and 251 μm (x -cut plates) were used for the THz and IR experiments. Spectra

of transmission and reflection coefficients of the prepared samples were measured using a set of spectrometers. Reflection coefficient spectra in the far-infrared and middle infrared ranges (frequencies 30–8000 cm^{-1}) were recorded with the resolution of 2 cm^{-1} using standard Fourier-transform infrared spectrometer Vertex 80v equipped with Hyperion 2000 microscope setup. In addition, we performed infrared transmission measurement in magnetic field up to 7 T using an Oxford Spectromag magneto-optical cryostat attached to the Fourier-transform spectrometer Bruker IFS 113v. At THz frequencies, $\nu = 8\text{--}100 \text{ cm}^{-1}$, time-domain TeraView spectrometer was used to directly determine the real ϵ' and imaginary ϵ'' parts of the complex dielectric permittivity $\epsilon^* = \epsilon' + i\epsilon''$ from the complex (amplitude and phase) transmission coefficient spectra, with the frequency resolution of 1 cm^{-1} . At even lower frequencies, down to 1.5 cm^{-1} , direct measurements of ϵ' and ϵ'' spectra were performed with a quasi-optical spectrometer based on monochromatic radiation generators with continuously tunable frequency (backward-wave oscillators) [39]. With the measured spectra of ϵ' and ϵ'' , THz reflection coefficient spectra were calculated using standard Fresnel equations and merged with the measured infrared reflection coefficient spectra. The spectral analysis of the so-obtained broad-band THz-IR reflectivity and transmissivity spectra *in combination* with the directly determined THz spectra of ϵ' and ϵ'' was performed, as is described below. As a result, temperature-dependent broad-band dielectric response of $\text{Ba}_{0.3}\text{Pb}_{0.7}\text{Fe}_{12}\text{O}_{19}$ was obtained for polarizations parallel and perpendicular to the crystallographic c axis, $\mathbf{E}||c$ and $\mathbf{E}\perp c$. The spectra were obtained at temperatures down to 6 K with open-cycle liquid helium optical cryostats. Here, we discuss the results obtained below 1000 cm^{-1} since above this frequency the spectra were featureless and corresponding reflectivity data were used to determine the high-frequency dielectric constant needed for the spectral analysis, as described below.

Radio-frequency dielectric measurements were performed in the $\mathbf{E}||c$ geometry at frequencies 40 Hz–10 MHz and at temperatures 4–300 K. The samples were prepared in the form of plane-parallel plates with typical dimensions 0.70 mm \times 0.65 mm \times 0.15 mm where the c axis was within the plate surfaces. To obtain the complex dielectric function we measured the complex conductance using an Agilent 4294A and Keysight E4980AL-102 impedance analyzers. The employed ac signal levels of 10 and 50 mV were confirmed to be well within the linear response regime. Repeated measurements using different contact materials (silver paint, amorphous carbon paint) and different sample geometries were performed in order to successfully resolve and separate intrinsic sample response from the extrinsic contributions due to contact resistances and surface layer Maxwell–Wagner relaxation [40, 41].

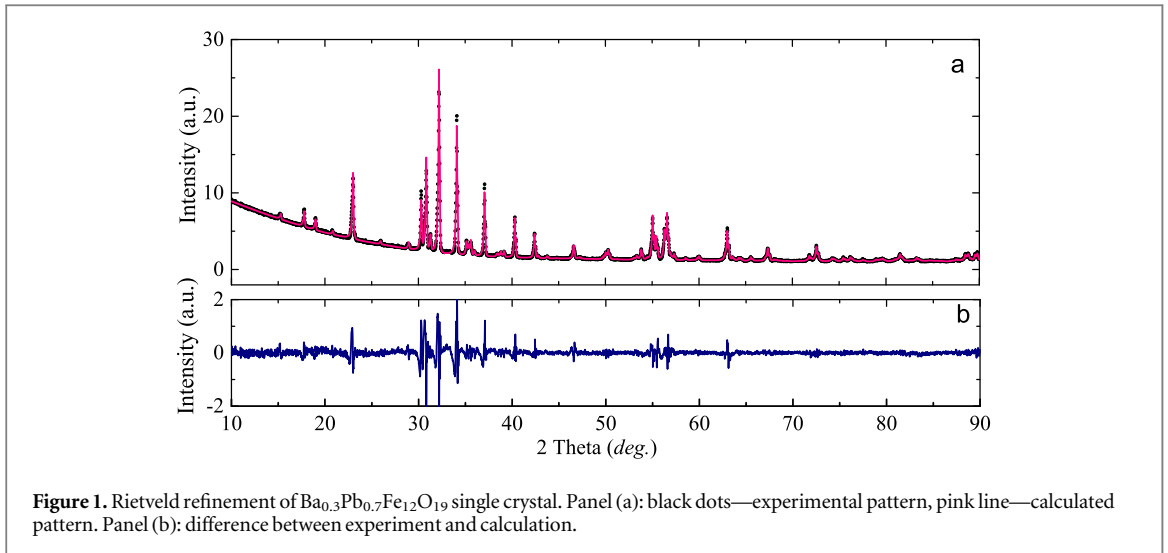
SQUID dc magnetization measurements under $H = 100 \text{ Oe}$ and for magnetic field orientation $\mathbf{H}||c$ displayed no difference between the zero-field-cooled and field-cooled data, as well as a virtually temperature-independent, saturated susceptibility from room temperature down to 2 K (not presented here), which suggests that the studied compound is a very soft ferromagnet at all studied temperatures. Therefore, low-amplitude ac magnetic measurements were performed at temperatures 4–300 K and in the frequency range 2 Hz–11 kHz, using a high-resolution home-made ac susceptibility system. As a nonlinear ferromagnetic response starts already above 0.5 Oe (not shown here) a very low ac magnetic excitation field of $H = 0.2 \text{ Oe}$ in the $\mathbf{H}||c$ geometry was used.

Heat capacity of the crystals was measured by the pulse 2τ method [42], separating the heat capacity contribution of the sample from the one of the holder. The sample holder consists of a thin foil heater (Vishay strain gage ED-DY-031DE-350) and the thermometer (Lake Shore Cernox CX-1050-BR) suspended on constantan 50 μm thin wires. Flat rectangular sample with a mass of 12.5 mg was fixed on a back side of the heater with a thin layer of GE varnish. The measurements have been performed in a high vacuum (better than 10^{-6} mbar) and in the temperature interval 4–315 K. The unit cell molar heat capacity c_p has been calculated based on the $Z = 2$ molar mass of $M = 2320.8 \text{ g mol}^{-1}$.

3. Results

3.1. Composition and XRD data

In a search for the optimal PbO flux content needed for crystal growth [36] it was found that when using 80 at% (atomic percent) of PbO the melting temperature is minimal and provides stable formation of the hexaferrite phase. Single crystals of up to 5 mm in size were grown. Concentrations of Fe, Ba and Pb in the samples were determined by EDX study to be 37.62, 0.96 and 2.18 at%, respectively, equivalent to the chemical formula $\text{Ba}_{0.3}\text{Pb}_{0.7}\text{Fe}_{12}\text{O}_{19}$. Comparison of our PXRD results with the literature XRD data [43, 44] clearly indicates the single-phase character of the magnetoplumbite-type structure of our crystals. Analysis of systematic absences and symmetry-equivalent reflections unambiguously indicated the hexagonal crystal symmetry with the space group $P6_3/mmc$ (N 194) and lattice parameters $a = 5.8911(20) \text{ \AA}$ and $c = 23.181(7) \text{ \AA}$ at $T = 300 \text{ K}$. We have processed the data and obtained the theoretical pattern of $\text{Ba}_{0.3}\text{Pb}_{0.7}\text{Fe}_{12}\text{O}_{19}$ and its Rietveld refinement using Rigaku PDXL software. As a result, we have $R_{wp} = 4.69\%$ and $R_p = 3.01\%$. The obtained patterns are shown



in figure 1 where black dots correspond to experiment, pink line—to calculation and blue line is the difference between experiment and calculation.

3.2. Terahertz and infrared spectroscopy results

The room temperature terahertz and infrared spectra of reflection and transmission coefficients and complex dielectric permittivity $\varepsilon^*(\nu) = \varepsilon'(\nu) + i\varepsilon''(\nu)$ of Ba_{0.3}Pb_{0.7}Fe₁₂O₁₉ for the $\mathbf{E}||c$ and $\mathbf{E}\perp c$ polarizations are shown in figure 2. At frequencies below 40 cm⁻¹, the spectra of transmission and reflection coefficients exhibit periodic oscillations due to the Fabry–Perot interference of the radiation within plane-parallel samples. These oscillations allow an additional way to determine the real and imaginary permittivities at the frequencies of maximal transmissivity, where the interaction of the probing radiation with the material is the most effective and the accuracy of the dielectric parameters determination is the best [44]; corresponding data are shown by stars. Interferometric effects disappear above approximately 40 cm⁻¹ due to increased absorption; here all spectral features are connected with absorption resonances. Broad-band spectra of real and imaginary dielectric permittivities were obtained by using a least-square procedure for a *combined* analysis of the spectra of THz and IR reflection coefficient spectra (with the THz reflection coefficients calculated basing on the directly measured ε' and ε'' as mentioned above), THz transmission coefficient spectra and the spectra of directly measured THz ε' and ε'' spectra. Transmission and reflection coefficients were modeled with well-known Fresnel expressions for optics of layered structures [45]. The dielectric absorption resonances were fitted with the Lorentzian expressions for complex dielectric permittivity:

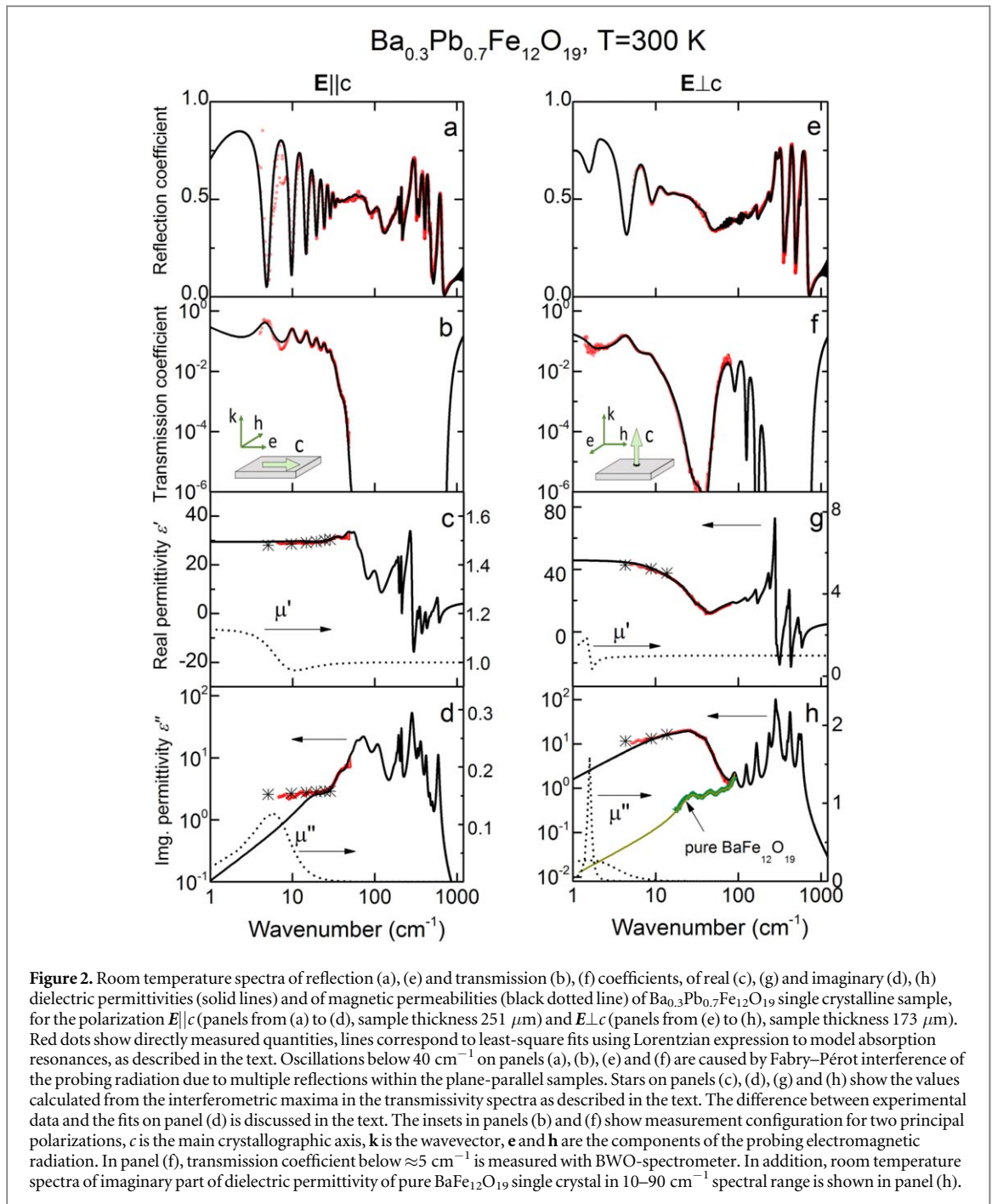
$$\varepsilon^*(\nu) = \varepsilon'(\nu) + i\varepsilon''(\nu) = \sum_j \frac{f_j}{\nu_j^2 - \nu^2 + i\nu\gamma_j} + \varepsilon_\infty, \quad (1)$$

where $f_j = \Delta\varepsilon_j\nu_j^2$ is the oscillator strength of the j th resonance, $\Delta\varepsilon_j$ is its dielectric contribution, ν_j represents the resonance frequency, γ_j is the damping factor and ε_∞ is the high-frequency dielectric constant that was determined from the reflectivity spectra measured up to 8000 cm⁻¹ (see electronic supplementary information available online at stacks.iop.org/NJP/21/063016/mmedia).

According to figure 2, the spectra for the two polarizations, $\mathbf{E}\perp c$ and $\mathbf{E}||c$, strongly differ by the number of the absorption resonances and their intensities. We associate narrow absorption lines in the infrared range with phonon modes. Their observed numbers are in agreement with the results of a factor group analysis that yields 17 E_{1u} modes active in the $\mathbf{E}\perp c$ polarization and 13 A_{2u} modes active in the $\mathbf{E}||c$ polarization [35], see below. For the $\mathbf{E}||c$ polarization, in the range 5–30 cm⁻¹ the experimentally measured values of ε'' significantly exceed the results obtained by fitting the spectra with Lorentzians, see figure 2(d). This is an indication of an extra absorption exceeding that of the lowest-frequency ‘tails’ of the IR phonons. Introducing an additional dielectric Lorentzian does not simultaneously fit $\varepsilon'(\nu)$ and $\varepsilon''(\nu)$ spectra together with the spectra transmission and reflection coefficients. The only way to satisfactorily reproduce these spectra was to introduce *magnetic* Lorentzian modes (see, e.g. in Mukhin *et al* [46]):

$$\mu^*(\nu) = \mu'(\nu) + i\mu''(\nu) = \sum_j \frac{\Delta\mu_j \cdot \nu_j^2}{\nu_j^2 - \nu^2 + i\nu\gamma_j}, \quad (2)$$

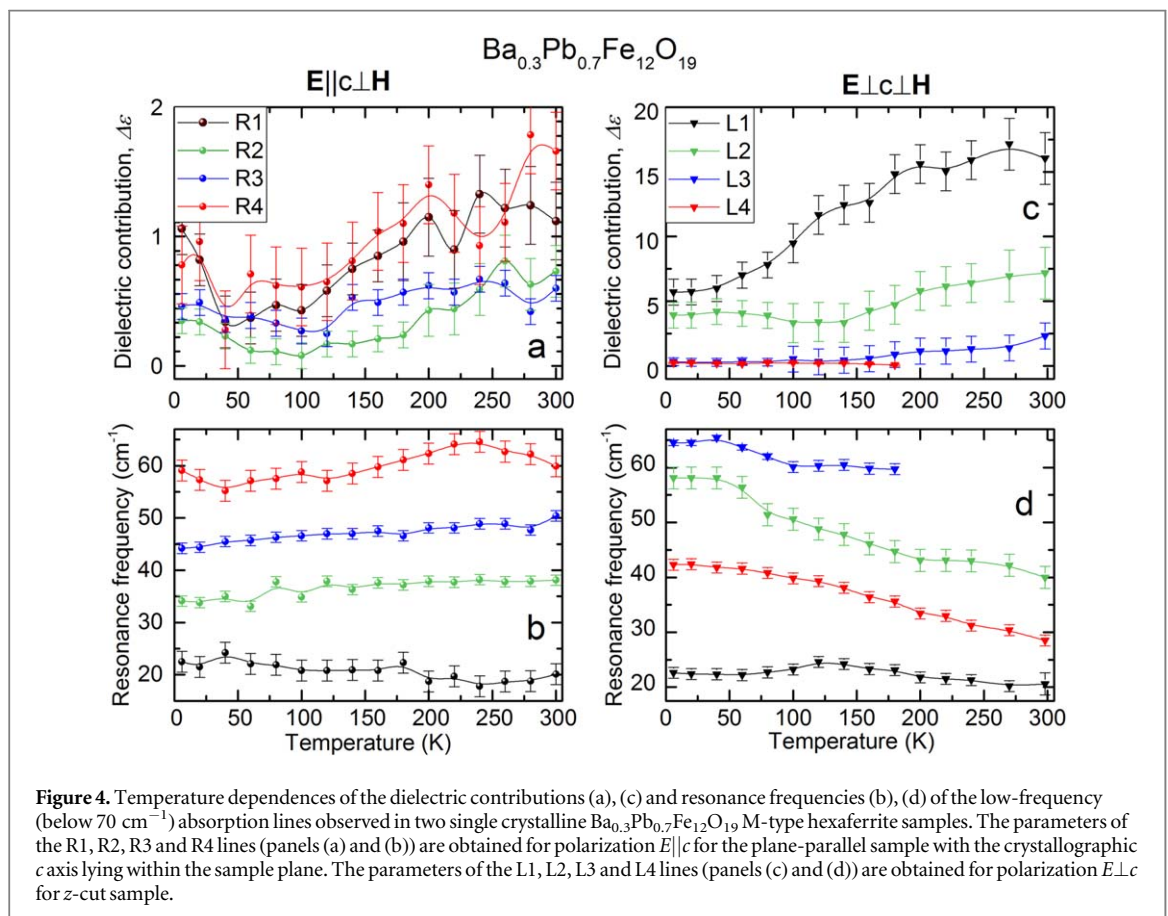
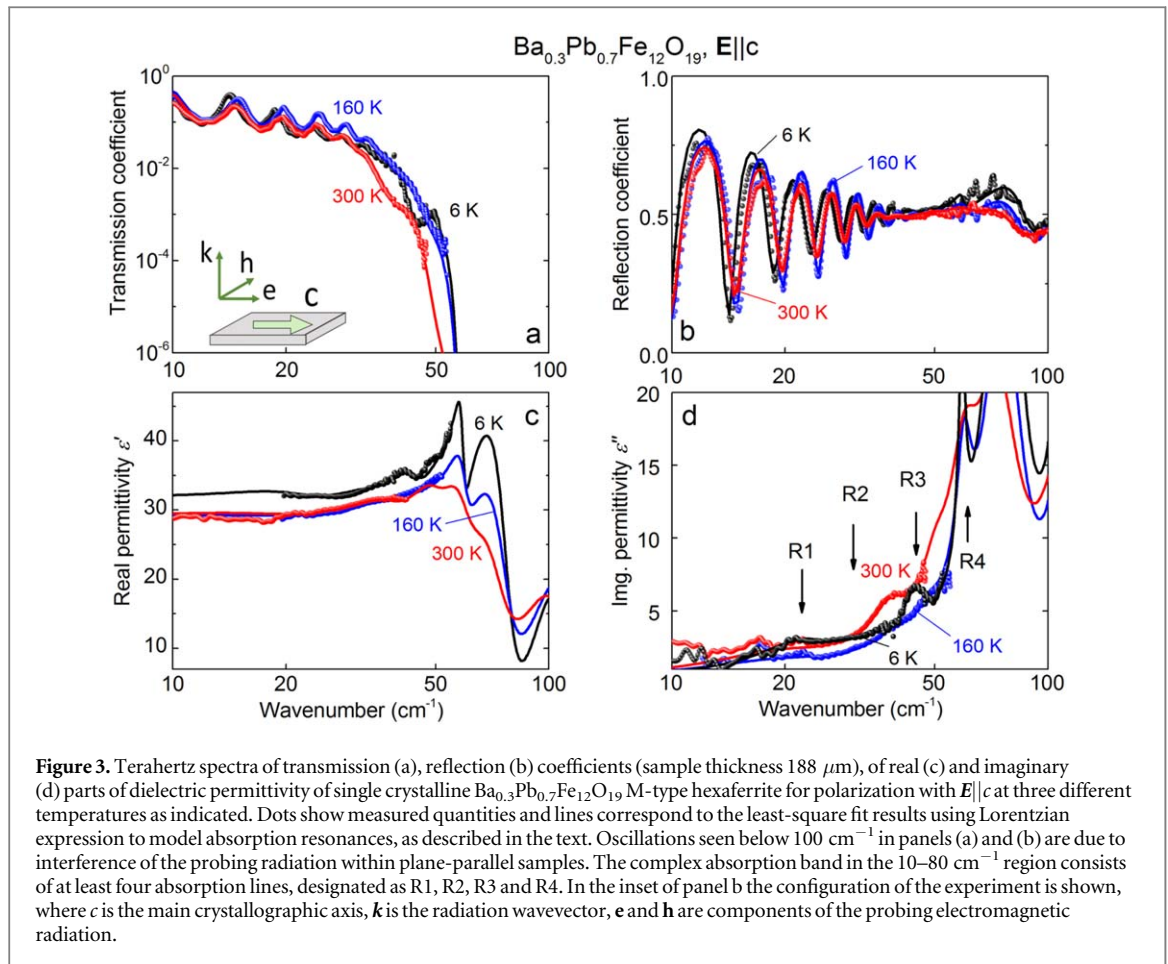
where $\Delta\mu_j$ is the magnetic contribution, ν_j is the resonance frequency and γ_j is the damping factor. The corresponding fitting results are represented by solid lines in figures 2(a), (b), and the so-obtained real and

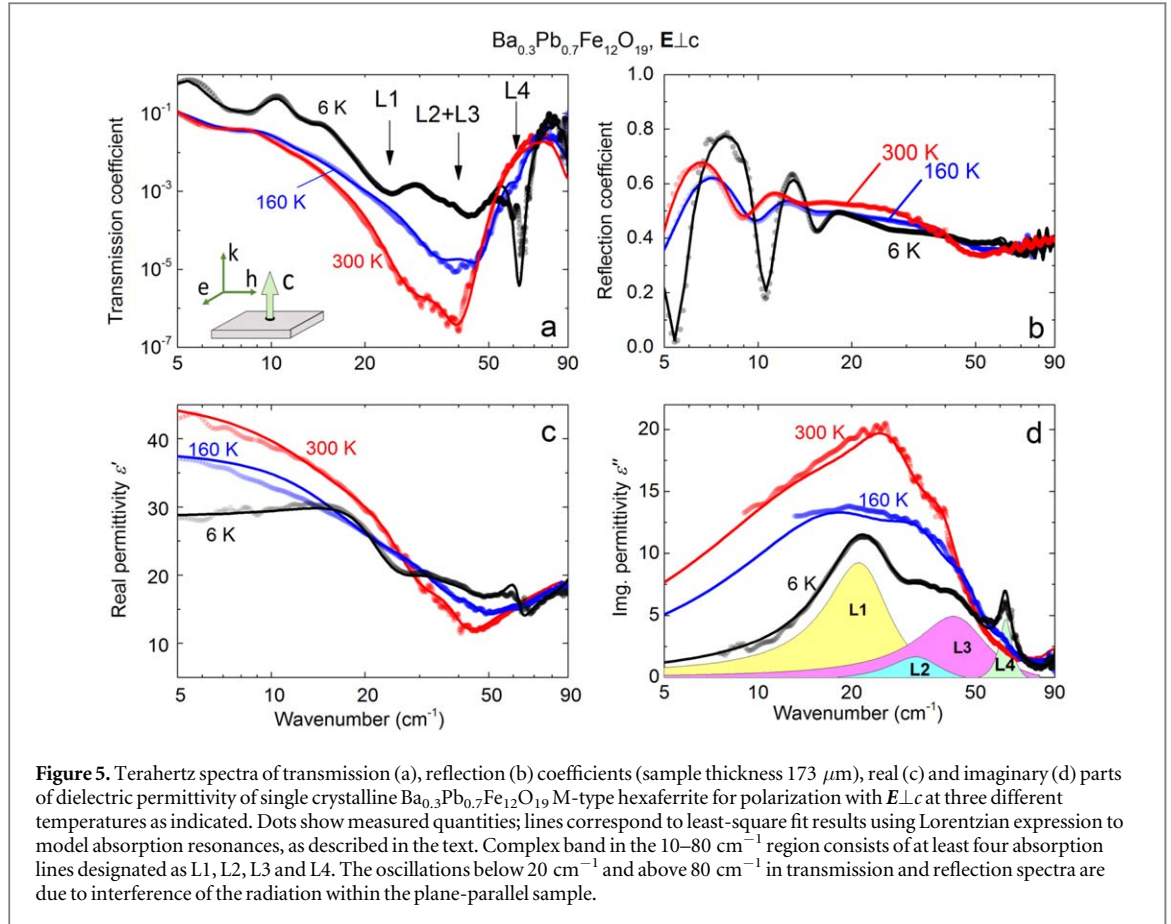


imaginary parts of magnetic permeability are shown by the dashed lines in figures 2(c), (d), indicating magnetic absorption line located at $7\ \text{cm}^{-1}$. Similarly, in the $E\perp c$ configuration, we have detected at least two extra magnetic absorption resonances at 1.5 and $2.4\ \text{cm}^{-1}$ (dashed lines in figures 2(g), (h)).

For the $E||c$ polarization, all $13\ A_{2u}$ phonon modes predicted by factor group analysis are resolved located above $70\ \text{cm}^{-1}$ already at $300\ \text{K}$. With decreasing temperature phonon lines get narrower and in addition extra absorption lines become clearer at $15\text{--}65\ \text{cm}^{-1}$, see figure 3. We consider these lines as dielectric in origin (see below) and analyze the spectra using Lorentzian expression (1). The analysis provides evidence for four resonances located at ≈ 22 (R1 resonance), ≈ 34 (R2), ≈ 45 (R3) and $\approx 59\ \text{cm}^{-1}$ (R4). The temperature behavior of dielectric contributions and resonant frequencies of this terahertz quadruplet is rather unusual as shown in figure 4.

The R2 and R3 modes (see figures 3 and 4) red-shift upon cooling, while the temperature dependences of the R1 and R4 modes positions show minimum and maximum, respectively, at around $250\ \text{K}$. The dielectric contributions of all the four modes reach maxima at $250\ \text{K}$ and minima at $100\ \text{K}$. We note that the combined dielectric contribution of the quadruplet is strongly temperature dependent: $\Delta\varepsilon_{\text{tot}}(300\ \text{K}) = 4.11$,





$\Delta\epsilon_{\text{tot}}(130 \text{ K}) = 1.64$, $\Delta\epsilon_{\text{tot}}(6 \text{ K}) = 2.65$; this might mean certain charge transfer between related degrees of freedom.

A distinct set of absorption lines is observed also for the perpendicular polarization, $\mathbf{E} \perp \mathbf{c}$, see figures 2(e)–(h). The infrared phonon modes reveal small changes in their frequency positions (by $5\text{--}6 \text{ cm}^{-1}$), damping factors and dielectric contributions. Changes of the parameters of the THz modes are significantly more pronounced. A broad minimum in the transmission coefficient is observed between 10 and 80 cm^{-1} . Its complex shape can be reproduced by involving at least four absorption lines (modeled with expression 1) which become clearly resolved at 6 K , as shown in figure 5. This figure shows in details the low-frequency response for the polarization $\mathbf{E} \perp \mathbf{c}$ at three temperatures: 300 , 160 and 6 K . Four resonances, L1–L4, are resolved in the spectra. On cooling, the L2, L3, L4 peaks show certain blue-shift until the plateau in their frequencies behavior is reached at $50\text{--}80 \text{ K}$, while the frequency of the L1 resonance exhibits a maximum around 130 K . A similar behavior is detected for the dielectric contributions of the peaks, which decrease on cooling and saturate around the same temperature of $50\text{--}80 \text{ K}$, except for the L2 peak whose $\Delta\epsilon(T)$ shows a shallow dip around 130 K . The L4 resonance is resolved only below 180 K . The combined dielectric contribution of the quadruplet decreases by half when the temperature is reduced from 300 to 6 K : $\Delta\epsilon_{\text{tot}}(300 \text{ K}) = 26.47$, $\Delta\epsilon_{\text{tot}}(6 \text{ K}) = 10.22$ also showing possible charge transfer between excitations.

3.3. AC magnetic susceptibility and dielectric properties

The complex ac magnetic susceptibility $\chi = \chi' - i\chi''$ of $\text{Ba}_{0.3}\text{Pb}_{0.7}\text{Fe}_{12}\text{O}_{19}$ is shown in figure 6 together with the solid lines representing the least-square fits to the Cole–Cole expression

$$\chi = \Delta\chi / [1 + (i\omega\tau_0)^{1-\alpha}], \quad (3)$$

where $\Delta\chi$ is the ac susceptibility strength, τ_0 the mean relaxation time, and $1 - \alpha$ describes the distribution width of the relaxation times, see figure 7. The magnetic relaxation strength does not depend on temperature which implies that the number of responding magnetic entities remains constant. At the same time, the mean relaxation time of the overdamped response $\tau_0 = 1/2\pi f_p$ follows an Arrhenius-type behavior $\tau_0 \propto \exp(W/k_B T)$, where f_p corresponds to the loss peak frequency, $W \approx 100 \text{ meV}$ is the activation energy and k_B is the Boltzmann constant. Such an activated ac magnetic response is characteristic for the slowing down of domain-wall dynamics in ferromagnets [47]. Therefore, we assign the observed dispersive magnetic response to the thermally-activated dynamics of domain walls, associated with the underlying magnetic structure.

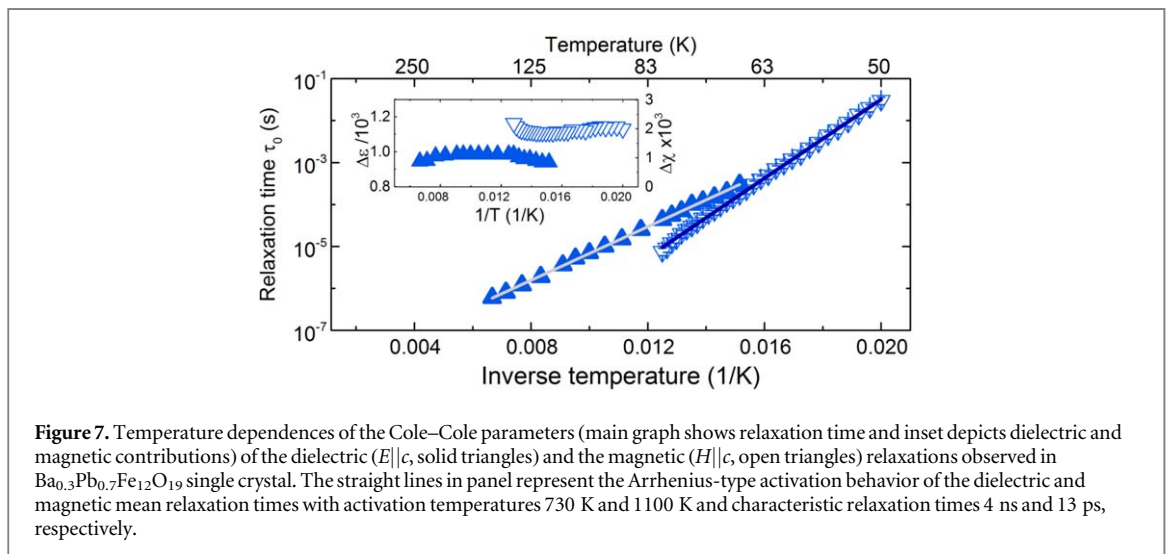
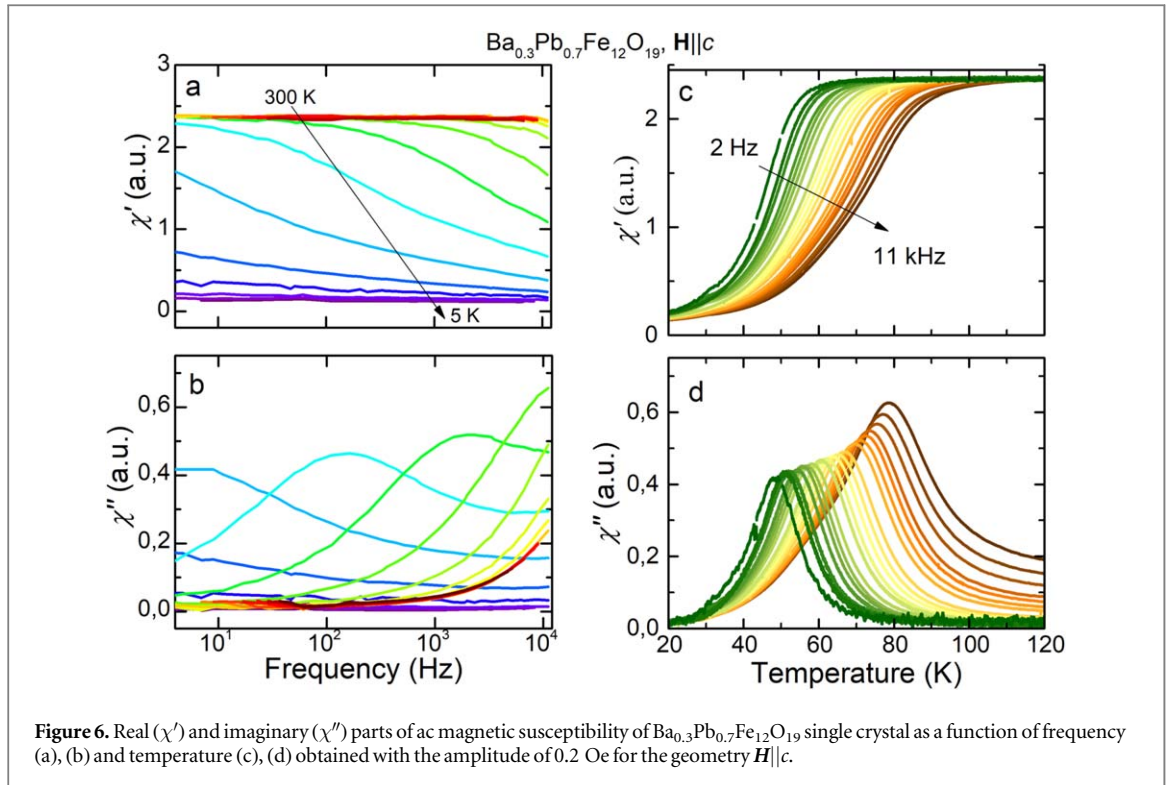
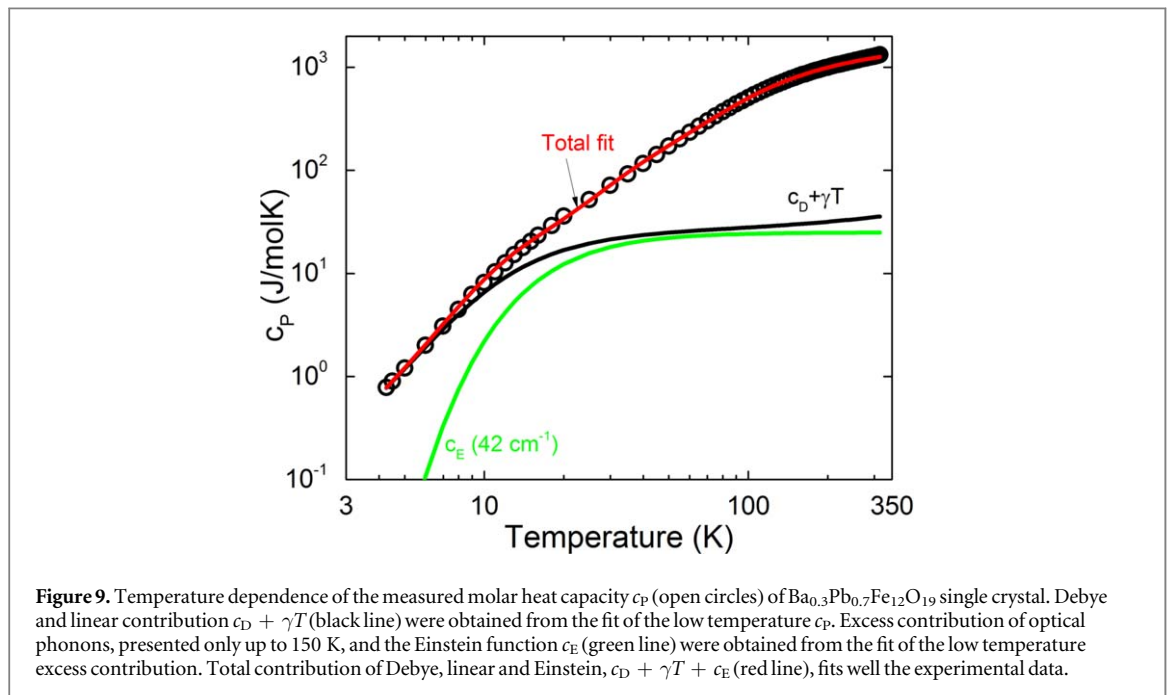
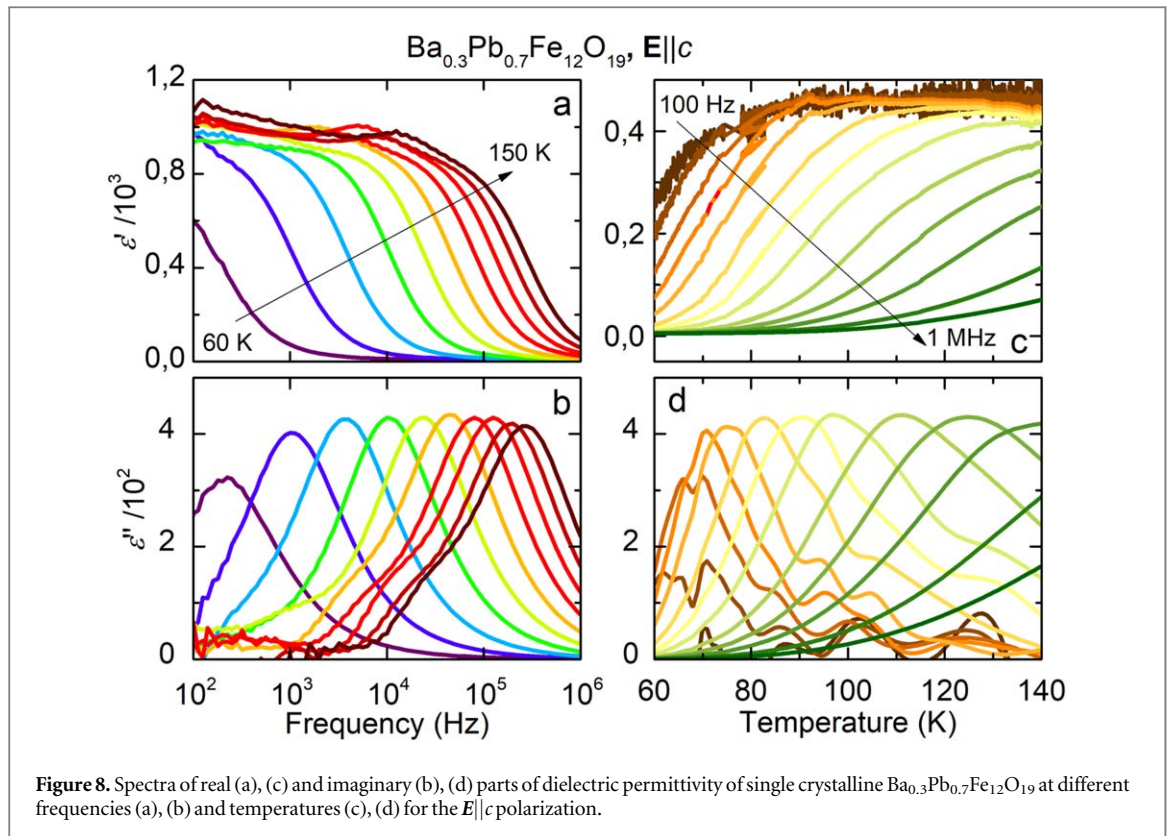


Figure 8 shows the low-frequency complex dielectric response of the compound. As can be seen from figure 7, the obtained dielectric relaxation time follows a very similar activation behavior as the one of the magnetic response, both in activation energies and in their absolute values. In glassy systems that follow the Arrhenius gradual slowing down instead of Vogel–Fulcher type behavior, a glass transition temperature T_g is commonly defined as the temperature where the characteristic relaxation time τ_0 extrapolates to the value of 100 s [48]. In our case, for dielectric and ac magnetic response we get very close values of $T_g \approx 30$ K and 36 K, respectively. Furthermore, the temperature independence of the dielectric contribution implies that the number of responding dipolar entities does not change. Therefore, in the covered temperature range the low-frequency response of $\text{Ba}_{0.3}\text{Pb}_{0.7}\text{Fe}_{12}\text{O}_{19}$ points to a bi-relaxor-like mechanism in which both dielectric and magnetic responses stem from the same overdamped dynamics related to the magnetic domain walls.

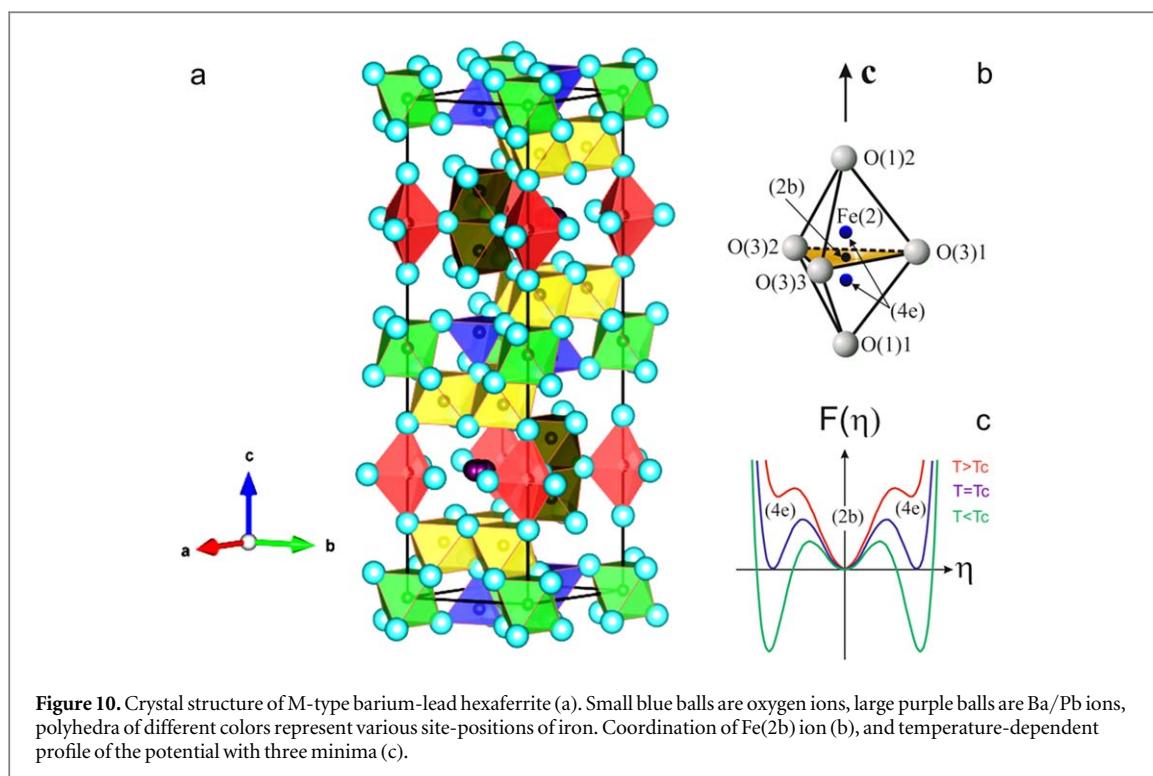
3.4. Heat capacity

To check whether significant changes in the absorption lines parameters could be caused by a phase transition, the heat capacity of $\text{Ba}_{0.3}\text{Pb}_{0.7}\text{Fe}_{12}\text{O}_{19}$ was measured with the results presented in figure 9. The temperature



dependence of c_p does not show any feature that could indicate a phase transition. At the highest temperatures the heat capacity approaches the Dulong–Petit limit, whereas at the lowest temperatures it can be well approximated by the Debye-type βT^3 contribution of acoustic phonons [49] together with a weak linear contribution $\sim \gamma T$. The Debye temperature of 61.6 K estimated from β corresponds to the acoustic mode frequency of about 43 cm^{-1} . The combined Debye (c_D) and the linear contributions are represented by the solid line in figure 9.

The remaining contribution from optical phonons $c_p - c_D - \gamma T$ is fitted to contributions of the remaining 63 optical modes, each representing a set of 1 longitudinal and two transversal optical modes that are dispersionless and isotropic and having Dulong–Petit contribution of $3R$ at high temperatures. Therefore, the contribution of



each mode is approximated by the Einstein expression c_E (dashed line) in the whole temperature range [49] with the lowest oscillator frequency of 42 cm^{-1} . This value is, however, somewhat lower than the highest acoustic mode obtained by the Debye term, which is probably a consequence of the approximation: as the heat capacity is a cumulative and not selective technique, it is hard to obtain subtle differences, such as phonon dispersion, etc. The remaining contributions to the heat capacity stem from optical modes that are distributed between 100 and 1000 cm^{-1} (not shown here).

The origin of the linear term cannot be ascribed to free charge carriers since the system is an insulator. We assume that it can stem from possible polaronic transport.

4. Discussion

4.1. Origin of terahertz resonances

Let us compare the dielectric response obtained for $\text{Ba}_{0.3}\text{Pb}_{0.7}\text{Fe}_{12}\text{O}_{19}$ single crystal with that of single crystalline $\text{BaFe}_{12}\text{O}_{19}$ (BaM). First detailed study of terahertz-infrared dynamics of pure BaM was reported by Mikheykin *et al* [50] and the results showed no intensive absorption below 90 cm^{-1} frequency region. In the room temperature spectra of imaginary part of dielectric permittivity of pure BaM (figure 2, panel (h)), in the range $10\text{--}90 \text{ cm}^{-1}$ four very weak lines are detected at nearly the same positions as in lead-substituted $\text{Ba}_{0.3}\text{Pb}_{0.7}\text{Fe}_{12}\text{O}_{19}$. We assign the origin of these lines to electronic transitions within the fine-structured Fe^{2+} ground state. The intensive absorption of the same lineshape is detected in Ti-substituted $\text{BaFe}_{12}\text{O}_{19}$ [51]. As could be seen from the investigation of compounds with different concentration of Pb^{2+} , the intensity of the absorption growth with increasing the lead content in the crystal lattice (see [35, 50, 52] and figure 3 in the ESI). Both observations confirm our assignment.

The structure of the M-type hexaferrites is of the magnetoplumbite type (space group $P6_3/mmc$) with $Z = 2$, i.e. the unit cell contains two formula units (total 64 ions). The crystal lattice consists of layers oriented normal to the c axis, with four alternating structural blocks of cubic and hexagonal packings. The largest cation (Ba^{2+} , Pb^{2+} or Sr^{2+}) occupies 12-coordinated 2d Wyckoff site-position, and the Fe^{3+} ions occupy 5 distinct site-positions with different spin orientations—five-coordinated trigonal bi-pyramidal 2b, three non-equal octahedral 12k, 2a and 4f₂, and one tetrahedral 4f₁ [53], see figure 10. A specific feature of the crystal structure of the M-type hexaferrites is the presence of ten-layered closely packed O_4 and Ba/PbO₃ sheets in the 2(h_3c_2) stacking, where iron ions occupy octahedral and tetrahedral voids. Hexagonally packed h-layers (so-called R slabs) fuse with S-blokes that have cubic c-packing. Such packing is characteristic for the structural type of spinel (magnetite $\text{Fe}_3\text{O}_4 \sim \text{Fe}^{2+}\text{Fe}^{3+}_3\text{O}_4$), in which the tetrahedral positions [$\text{Fe}(4f_2)$] are usually occupied by divalent iron ions, and the octahedral positions [$\text{Fe}(2a)$]—by divalent and trivalent iron ions. The presence of Fe^{2+} ions

in polycrystalline $\text{BaFe}_{12}\text{O}_{19}$ was confirmed by XPS study [54] and by chemical analysis in single crystals of $\text{BaFe}_{12}\text{O}_{19}$ and $\text{PbFe}_{12}\text{O}_{19}$ [55]. A small oxygen non-stoichiometry in the compounds can serve as ‘source’ of Fe^{2+} ions in our samples. According to Pullar [56], the concentration of divalent iron throughout the volume of the crystalline grain is large at grain boundaries, and, as a consequence, its total concentration is expected to be larger in polycrystals rather than in single crystalline samples. A higher growth temperature also leads to an increase of Fe^{2+} content.

The determined dielectric contributions of the THz absorption lines are by more than an order of magnitude larger than in BaM, indicating much lower concentration of Fe^{2+} in pristine samples. We conclude, that the growth processes from oxides, initially containing divalent iron, and the presence of various micro-defects in the crystal lattice (e.g. boundary distortions, oxygen vacancies) unavoidably result in an incorporation into site-positions of the lattice of small amounts of divalent iron. This was also shown by Pattanayak [54] for polycrystalline sample and confirmed by our terahertz spectroscopy on single crystalline BaM. Nevertheless, considering the suggested mechanisms that lead to the presence of Fe^{2+} in BaM is definitely not sufficient to explain the tremendous dielectric contribution to low-energy dielectric constant in $\text{Ba}_{0.3}\text{Pb}_{0.7}\text{Fe}_{12}\text{O}_{19}$ single crystals. We believe that there must be additional sources of divalent iron in lead-substituted hexaferrite, like the presence of lead ions with two lone electrons in the 6s orbital. We thus assume that lead can share two electrons with the nearest trivalent iron ions reducing them to the divalent state.

The Fe^{2+} high-spin ground state ${}^5\text{D}({}^5\text{E})$ with degeneracy of 10 is split by the second-order spin-orbit interactions with ${}^5\text{T}_2$ state. The ${}^5\text{D}({}^5\text{T}_2)$ state is split into five equidistant levels with degeneracy 1, 3, 2, 3 and 1 separated by $10\text{--}15\text{ cm}^{-1}$ [57, 58]. Our spectra reveal four resonances in the region $20\text{--}65\text{ cm}^{-1}$ that are assigned to electronic transitions of Fe^{2+} ions. We note that similar THz response connected with the Fe^{2+} electronic transitions was observed in beryl crystals by Shakurov *et al* [59]. Our THz transmissivity measurements of $\text{Ba}_{0.3}\text{Pb}_{0.7}\text{Fe}_{12}\text{O}_{19}$ samples in external magnetic field up to 7 T (not presented) did not reveal any significant shift or quenching of the quadruplet spectral components, ruling out purely magnetic (magnon) or mixed-type (electro-magnon) origin of these resonances.

According to the crystal field theory, the crystal field parameter $10Dq$ and the parameter λ of effective spin-orbit interaction between the ${}^5\text{E}$ and ${}^5\text{T}_2$ terms lead to the splitting K between the levels:

$$K = \frac{6\lambda^2}{10Dq}. \quad (4)$$

Assuming $\lambda \approx 100\text{ cm}^{-1}$, the value that equals that of the free ion and close to the values obtained for selenides [57, 60], the crystal field strength is estimated to be $10Dq \approx 5000\text{ cm}^{-1}$, which is in a reasonable agreement with the expected values in the range $2000\text{--}6000\text{ cm}^{-1}$ [57, 58, 61].

As to the lowest temperature behaviors of the observed THz resonances, we suggest that the pronounced change of their parameters around $50\text{--}70\text{ K}$ is a manifestation of an order-disorder phenomena connected with the iron ions that occupy 5-coordinated bi-pyramidal position 2b. According to Muller and Collomb [62], this bi-pyramidal position is split into two tetrahedral 4e positions. At relatively high temperatures, the Fe ions oscillate between the two tetrahedra, while at low enough temperatures they ‘freeze’ in the mirror planes of a bipyramid. We suggest, however, that both, the bi-pyramidal and the two distorted tetrahedral positions coexist. Corresponding potential profile of the ions should then have three minima for each of the three positions, see figures 10(b), (c). At low temperatures, due to the transformation of the potential, the Fe ions are frozen in one of the minima and have not enough energy to jump to the other split position, as shown in figure 10. More detailed description of this model is given in the work by Mikheykin *et al* [50].

4.2. Nature of radio-frequency response

We associate the observed radio-frequency relaxational response of $\text{Ba}_{0.3}\text{Pb}_{0.7}\text{Fe}_{12}\text{O}_{19}$ with the dynamics of polar magnetic domains walls. According to figure 7, the kHz–MHz dielectric relaxation and Hz–kHz magnetic relaxation are characterized by close values of activation energies and freezing temperatures of electric and magnetic dipoles. This allows us to suggest that these two relaxations stem from same process that reflects intertwined ferroelectric and magnetic orders. Such relaxation process can involve dynamics of differently directed spins of Fe^{3+} ions at the opposite 4e positions in the bipyramid. In such a case both, electric and magnetic ac field of the probing electromagnetic radiation would trigger ionic hopping between the two 4e states, in agreement with the experiment. The observed RF response is reminiscent of systems such as glasses [63] that exhibit the boson peak excitation and α -process relaxation in THz and RF ranges, or density wave systems [64–67] with pinned phason mode in the GHz–THz range and an overdamped phason relaxation in the RF range. We can thus suggest that the origin of the RF dispersion observed in $\text{Ba}_{0.3}\text{Pb}_{0.7}\text{Fe}_{12}\text{O}_{19}$ could be connected with the α -relaxation typical for glassy systems and relaxor ferroelectrics [67].

5. Conclusions

We present the results of the first systematic investigation of electromagnetic properties of single crystalline M-type hexaferrite $\text{Ba}_{0.3}\text{Pb}_{0.7}\text{Fe}_{12}\text{O}_{19}$ in an extremely broad frequency interval ranging from radio up to middle infrared frequencies. In the measured dielectric response spectra, we discover features that are typical for bi-relaxor-like systems; these are two relaxations, dielectric and magnetic, that coexist within the same temperature range. We suggest that both relaxations stem from the same glassy process of slowing down of magnetic domain dynamics. The terahertz response of the compound is shown to be governed by electronic transitions within the fine-structured ground state of divalent iron which is not supposed to exist according to charge-balance reasons and reveals itself in the spectra due to magnetostriction and electron–phonon interactions. We interpret the observed phenomena considering on a molecular level the influence of divalent lead on electrostatics of the substituted barium hexaferrite. Our results demonstrate critical sensitivity of fundamental properties of hexaferrites to the chemical composition which can result in drastically different properties of isostructural compounds. The obtained data pave the way to further studies of multiferroicity in the class of M-type hexagonal ferrites, the family of compounds that are prospective for use in emerging advanced terahertz electronic devices and components.

Acknowledgments

The work was supported by the Ministry of Education and Science of the Russian Federation (Projects 5 top 100, RFMEFI59417X0014), Grants RSCF 18-32-00663 and 19-12-00317, RFBR 17-02-01247, SFU grant VnGr -07/2017-23. Measurements were performed using equipment of MIPT Shared Facilities Center. DRG, TI and ST acknowledge the support by the Croatian Science Foundation project IP-2013-11-1011. DD acknowledges the support of the FemtoBias project, the Grant Agreement 55 of the NEWFELPRO fellowship project (Grant Agreement No. 291823) cofinanced by the EU 7th Framework Programme 2007–2013 (MSCA-FP7-PEOPLE-2011-COFUND). In SUSU, the work was supported by Act 211 Government of the Russian Federation, contract № 02.A03.21.0011, by the Ministry of Education and Science of the Russian Federation (4.1346.2017/4.6), and by the Russian Foundation for Basic Research (№ 19-53-04010).

Conflicts of interest

There are no conflicts to declare.

Authors contribution

Synthesis and characterization of the crystals was done by Chelyabinsk group (DAV, SAG). Moscow team (LNA, ESZ, ASP, BPG) carried out terahertz, sub-terahertz measurements and full analysis, Zagreb team (ST, TI, NN, DD and DS) provided ac susceptibility and dielectric experiments in RF range and heat capacity investigation, Ljubljana department (ZJ) worked on dc magnetization experiments. FIR temperature measurements were done in Stuttgart (LNA, MD). LNA, VIT, ASP, MD and BPG performed theoretical analysis of the results. DAZ made the analysis of diffractogram. LNA wrote the original manuscript with help of VIT and BPG. ASP and MD edited the manuscript, BPG directed the project. All authors discussed results and reviewed the manuscript.

ORCID iDs

Liudmila N Alyabyeva  <https://orcid.org/0000-0001-8238-4674>

Elena S Zhukova  <https://orcid.org/0000-0002-5482-9477>

Denis A Vinnik  <https://orcid.org/0000-0002-5190-9834>

Anatoliy S Prokhorov  <https://orcid.org/0000-0002-5688-682X>

Svetlana A Gudkova  <https://orcid.org/0000-0002-3028-947X>

Tomislav Ivek  <https://orcid.org/0000-0003-2638-9109>

Silvia Tomić  <https://orcid.org/0000-0001-9295-6736>

Damir Dominko  <https://orcid.org/0000-0003-2818-0771>

Martin Dressel  <https://orcid.org/0000-0003-1907-052X>

Dmitry A Zherebtsov  <https://orcid.org/0000-0002-3368-9858>

Boris P Gorshunov  <https://orcid.org/0000-0001-8882-3930>

References

- [1] Aminoff G 1925 Über ein neues oxydisches Mineral aus Långban *GFF* **47** 283–9
- [2] Özgür Ü, Alivov Y and Morkoç H 2009 Microwave ferrites, part 1: fundamental properties *J. Mater. Sci., Mater. Electron.* **20** 789–834
- [3] Chen D, Liu Y, Li Y, Yang K and Zhang H 2013 Microstructure and magnetic properties of Al-doped barium ferrite with sodium citrate as chelate agent *J. Magn. Magn. Mater.* **337–338** 65–9
- [4] Dhage V N, Mane M L, Keche A P, Birajdar C T and Jadhav K M 2011 Structural and magnetic behaviour of aluminium doped barium hexaferrite nanoparticles synthesized by solution combustion technique *Physica B* **406** 789–93
- [5] Harward I et al 2013 Physical properties of Al doped Ba hexagonal ferrite thin films *J. Appl. Phys.* **113** 043903
- [6] Pieper M W, Morel A and Kools F 2002 NMR analysis of La + Co doped M-type ferrites *J. Magn. Magn. Mater.* **242–245** 1408–10
- [7] Mariño-Castellanos P A, Anglada-Rivera J, Cruz-Fuentes A and Lora-Serrano R 2004 Magnetic and microstructural properties of the Ti^{4+} -doped Barium hexaferrite *J. Magn. Magn. Mater.* **280** 214–20
- [8] Haijun Z, Zhichao L, Chenliang M, Xi Y, Liangying Z and Mingzhong W 2003 Preparation and microwave properties of Co- and Ti-doped barium ferrite by citrate sol-gel process *Mater. Chem. Phys.* **80** 129–34
- [9] Tsutaoka T and Koga N 2013 Magnetic phase transitions in substituted barium ferrites $BaFe_{12-x}(Ti_{0.5}Co_{0.5})_xO_{19}$ ($x = 0-5$) *J. Magn. Magn. Mater.* **325** 36–41
- [10] Teh G B, Saravanan N and Jefferson D A 2007 A study of magnetoplumbite-type (M-type) cobalt-titanium-substituted barium ferrite, $BaCo_xTi_xFe_{12-2x}O_{19}$ ($x = 1-6$) *Mater. Chem. Phys.* **105** 253–9
- [11] Sláma J, Grusková A, Papánová M, Kevická D, Jančárik V, Dosoudil R, Mendoza-Suárez G and González-Angeles A 2005 Properties of M-type barium ferrite doped by selected ions *J. Electr. Eng.* **56** 21–5
- [12] Mariño-Castellanos P A, Moreno-Borges A C, Orozco-Melgar G, García J A and Govea-Alcaide E 2011 Structural and magnetic study of the Ti^{4+} -doped barium hexaferrite ceramic samples: theoretical and experimental results *Physica B* **406** 3130–6
- [13] Mallick K K, Shepherd P and Green R J 2007 Magnetic properties of cobalt substituted M-type barium hexaferrite prepared by coprecipitation *J. Magn. Magn. Mater.* **312** 418–29
- [14] Vinnik D A, Ustinov A B, Zharebtsov D A, Vitko V V, Gudkova S A, Zakharchuk I, Lähderanta E and Niewa R 2015 Structural and millimeter-wave characterization of flux grown Al substituted barium hexaferrite single crystals *Ceram. Int.* **41** 12728–33
- [15] Guerrero A L, Mirabal-García M, Palomares-Sánchez S A and Martínez J R 2016 Effect of pb on the magnetic interactions of the M-type hexaferrites *J. Magn. Magn. Mater.* **399** 41–5
- [16] Tan G L and Li W 2015 Ferroelectricity and ferromagnetism of M-type lead hexaferrite *J. Am. Ceram. Soc.* **98** 1812–7
- [17] Parkin I P, Elwin G, Kuznetsov M V, Pankhurst Q A, Bui Q T, Forster G D, Barquín L F, Komarov A V and Morozov Y G 2001 Self-propagating high temperature synthesis of $MFe_{12}O_{19}$ ($M = Sr, Ba$) from the reactions of metal superoxides and iron metal *J. Mater. Process. Technol.* **110** 239–43
- [18] Prathap S and Madhuri W 2017 Multiferroic properties of microwave sintered $PbFe_{12-x}O_{19-\delta}$ *J. Magn. Magn. Mater.* **430** 114–22
- [19] Lee S E, Kim H J, Lee J H, Oh K S, Hahn H T and Choi J W 2017 Magnetodielectric hexaferrite flake/polymer substrate for implantable antenna with an enhanced insensitivity to implant position *Mater. Lett.* **187** 94–7
- [20] Pignard S, Vincent H, Flavin E and Boust F 2003 Magnetic and electromagnetic properties of RuZn and RuCo substituted $BaFe_{12}O_{19}$ *J. Magn. Magn. Mater.* **260** 437–46
- [21] Afghahi S S S, Jafarian M and Stergiou C A 2016 X-band microwave absorbing characteristics of multicomponent composites with magnetodielectric fillers *J. Magn. Magn. Mater.* **419** 386–93
- [22] Jazirehpour M and Shams M H 2017 Microwave absorption properties of Ba–M Hexaferrite with high substitution levels of Mg–Ti in X band *J. Supercond. Nov. Magn.* **30** 171–7
- [23] Randa M and Priyono A 2016 *Proc.—2015 Int. Conf. on Radar, Antenna, Microwave, Electronics, and Telecommunications, ICRAMET 2015* pp 46–9
- [24] Korolev K A, Chen S, Barua R, Afsar M N, Chen Y and Harris V G 2017 Millimeter wave transmittance/absorption measurements on micro and nano hexaferrites *AIP Adv.* **7** 056101
- [25] Kumar S, Datt G, Santhosh Kumar A and Abhyankar A C 2016 Enhanced absorption of microwave radiations through flexible polyvinyl alcohol-carbon black/barium hexaferrite composite films *J. Appl. Phys.* **120** 164901
- [26] Ansari F, Soofivand F and Salavati-Niasari M 2015 Utilizing maleic acid as a novel fuel for synthesis of $PbFe_{12}O_{19}$ nanoceramics via sol-gel auto-combustion route *Mater. Charact.* **103** 11–7
- [27] Mousavi Ghahfarokhi S E, Rostami Z A and Kazeminezhad I 2016 Fabrication of $PbFe_{12}O_{19}$ nanoparticles and study of their structural, magnetic and dielectric properties *J. Magn. Magn. Mater.* **399** 130–42
- [28] Singhal S, Namgyal T, Singh J, Chandra K and Bansal S 2011 A comparative study on the magnetic properties of $MFe_{12}O_{19}$ and $MAFe_{11}O_{19}$ ($M = Sr, Ba$ and Pb) hexaferrites with different morphologies *Ceram. Int.* **37** 1833–7
- [29] Baykal A, Yokuş S, Güner S, Güngüneş H, Sözeri H and Amir M 2017 Magneto-optical properties and Mössbauer investigation of $BaSryPbzFe_{12}O_{19}$ hexaferrites *Ceram. Int.* **43** 3475–82
- [30] Kumar P, Gaur A and Kotnala R K 2017 Magneto-electric response in Pb substituted M-type barium-hexaferrite *Ceram. Int.* **43** 1180–5
- [31] Mao L, Cui H, An H, Wang B, Zhai J, Zhao Y and Li Q 2014 Stabilization of simulated lead sludge with iron sludge via formation of $PbFe_{12}O_{19}$ by thermal treatment *Chemosphere* **117** 745–52
- [32] Kostishyn V G, Panina L V, Timofeev A V, Kozhitov L V, Kovalev A N and Zyuzin A K 2016 Dual ferroic properties of hexagonal ferrite ceramics $BaFe_{12}O_{19}$ and $SrFe_{12}O_{19}$ *J. Magn. Magn. Mater.* **400** 327–32
- [33] Palomares-Sánchez S A, Ponce-Castañeda S, Martínez J R, Chumakov Y M, Leccabue F, Watts B E and Salazar-Ortiz R 2006 Structural analysis of barium hexaferrite embedded in an amorphous matrix *Mater. Lett.* **60** 1076–9
- [34] Díaz-Castañón E, Sánchez Ll S, Estevez-Rams J L, Leccabue F and Watts B E 1998 Magneto-structural properties of $PbFe_{12}O_{19}$ hexaferrite powders prepared by decomposition of hydroxide—carbonate and metal—organic precipitates *J. Magn. Magn. Mater.* **185** 194–8
- [35] Zhukova E S, Mikheykin A S, Torgashev V I, Bush A A, Yuzyuk Y I, Sashin A E, Prokhorov A S, Dressel M and Gorshunov B P 2016 Crucial influence of crystal site disorder on dynamical spectral response in artificial magnetoplumbites *Solid State Sci.* **62** 13–21
- [36] Vinnik D A et al 2017 Magnetic and structural properties of barium hexaferrite $BaFe_{12}O_{19}$ from various growth techniques *Materials* **10** 158
- [37] Moore P B, Gupta P K S and Le Page Y 1989 Magnetoplumbite, $Pb^{2+}Fe^{3+}_{12}O_{19}$: refinement and lone-pair splitting *Am. Mineral.* **74** 1186–94
- [38] Vinnik D A 2014 Resistive furnace for single crystals growth *Butlerov Commun.* **39** 2014

- [39] Gorshunov B, Volkov A, Spektor I, Prokhorov A, Mukhin A, Dressel M, Uchida S and Loidl A 2005 Terahertz BWO-spectroscopy *Int. J. Infrared Millim. Waves* **26** 1217–40
- [40] Ivek T, Korin-Hamzić B, Milat O, Tomić S, Clauss C, Dričko N, Schweitzer D and Dressel M 2011 Electrodynamic response of the charge ordering phase: dielectric and optical studies of α -(BEDT-TTF)₂I₃ *Phys. Rev. B* **83** 165128
- [41] Lunkenheimer P, Bobnar V, Bobnar V, Pronin A V, Pronin A V, Ritus A I, Volkov A A and Loidl A 2002 Origin of apparent colossal dielectric constants *Phys. Rev. B* **66** 521051–4
- [42] Hwang J S, Lin K J and Tien C 1997 Measurement of heat capacity by fitting the whole temperature response of a heat-pulse calorimeter *Rev. Sci. Instrum.* **68** 94–101
- [43] Shin H S and Kwon S-J 1992 A suggestion on the standard x-ray powder diffraction pattern of barium ferrite *Powder Diffr.* **7** 212–4
- [44] Dressel M and Grüner G 2003 *Electrodynamics of Solids: Optical Properties of Electrons in Matter* (Cambridge: Cambridge University Press) (<https://doi.org/10.1119/1.1516200>)
- [45] Born M and Wolf E 1999 *Principles of Optics* ed M Born and E Wolf 7th (expanded) edn (Cambridge: Cambridge University Press) p 952
- [46] Mukhin A, Gorshunov B, Dressel M, Sangregorio C and Gatteschi D 2001 Optical spectroscopy of crystal-field transitions in the molecular magnet Fe₈ *Phys. Rev. B* **63** 2144111–7
- [47] Prester M, Živković I, Drobač D, Šurija V, Pajić D and Berger H 2011 Slow magnetic dynamics and hysteresis loops of the bulk ferromagnet Co₇(TeO₃)₄Br₆ *Phys. Rev. B* **84** 064441
- [48] Rault J 2000 Origin of the Vogel–Fulcher–Tammann law in glass-forming materials: the α – β bifurcation *J. Non-Cryst. Solids* **271** 177–217
- [49] Kittel C 1996 *Introduction to Solid State Physics* 7th edn (New York: Wiley) p 689
- [50] Mikheykin A S, Zhukova E S, Torgashev V I, Razumnaya A G, Yuzyuk Y I, Gorshunov B P, Prokhorov A S, Sashin A E, Bush A A and Dressel M 2014 Lattice anharmonicity and polar soft mode in ferrimagnetic M-type hexaferrite BaFe₁₂O₁₉ single crystal *Eur. Phys. J. B* **87** 232
- [51] Alyabyeva L, Yegiyani S, Torgashev V, Zhukova E, Vinnik D, Prokhorov A, Gudkova S and Gorshunov B 2018 Polar soft mode in titanium-doped single crystalline BaFe_{12–x}Ti_xO₁₉ M-type hexaferrite *43rd Int. Conf. on Infrared, Millimeter, and Terahertz waves (IRMMW-THz) (Nagoya, 9–14 September)* pp 1–1 IEEE catalog o. CFP 181MM-ART
- [52] Alyabyeva L, Chechetkin A, Torgashev V, Zhukova E, Vinnik D, Prokhorov A, Gudkova S and Gorshunov B 2018 Terahertz-infrared electrodynamic studies of lead-doped single crystalline Ba_{1–x}Pb_xFe₁₂O₁₉ M-type hexagonal ferrite *43rd Int. Conf. on Infrared, Millimeter, and Terahertz waves (IRMMW-THz) (Nagoya, 9–14 September)* pp 1–1 IEEE catalog o. CFP 181MM-ART
- [53] Obradors X, Collomb A, Pernet M, Samaras D and Joubert J C 1985 X-ray analysis of the structural and dynamic properties of BaFe₁₂O₁₉ hexagonal ferrite at room temperature *J. Solid State Chem.* **56** 171–81
- [54] Pattanayak R, Panigrahi S, Dash T, Muduli R and Behera D 2015 Electric transport properties study of bulk BaFe₁₂O₁₉ by complex impedance spectroscopy *Physica B* **474** 57–63
- [55] Závěta K 1963 Anisotropy of the electrical conductivity of ferrites with the magnetoplumbite structure *Phys. Status Solidi* **3** 2111–8
- [56] Pullar R C 2012 Hexagonal ferrites: a review of the synthesis, properties and applications of hexaferrite ceramics *Prog. Mater. Sci.* **57** 1191–334
- [57] Slack G A, Roberts S and Ham F S 1967 Far-infrared optical absorption of Fe²⁺ in ZnS *Phys. Rev.* **155** 170–7
- [58] Vogel E E and Rivera-Iratchet J 1980 Interpretation of the far-infrared spectrum of Fe²⁺ in cubic CdTe and ZnS *Phys. Rev. B* **22** 4511–22
- [59] Shakurov G S, Khaibullin R I, Tomas V G, Fursenko D A, Mashkovtsev R I, Lopatin O N, Nikolaev A G, Gorshunov B P and Zhukova E S 2017 Submillimeter ESR spectra of Fe²⁺ ions in synthetic and natural beryl crystals *Phys. Solid State* **59** 1600–6
- [60] Moore C E 1958 *Atomic Energy Levels* vol III (Amsterdam: Elsevier) vol 3
- [61] Lever A B P 1984 *Inorganic Electronic Spectroscopy* (Amsterdam: Elsevier) p 863
Lever A B P 1985 *Inorganic Electronic Spectroscopy* (New York: Elsevier)
- [62] Muller J and Collomb A 1992 A new representation of the bipyramidal site in the SrFe₁₂O₁₉ M-type hexagonal ferrite between 4.6 and 295 K *J. Magn. Magn. Mater.* **103** 194–203
- [63] Angell C A 1995 Formation of glasses from liquids and biopolymers *Science* **267** 1924–35
- [64] Littlewood P B 1987 Screened dielectric response of sliding charge-density waves *Phys. Rev. B* **36** 3108
- [65] Grüner G 1988 The dynamics of charge-density waves *Rev. Mod. Phys.* **60** 1129
- [66] Starešinić D et al 2002 Wide-temperature-range dielectric response of the charge-density-wave system TaS₃ *Phys. Rev. B* **65** 165109
- [67] Cross L E 1987 Relaxor ferroelectrics *Ferroelectrics* **76** 241